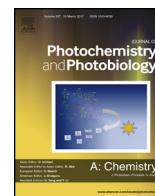




Contents lists available at ScienceDirect

Journal of Photochemistry and Photobiology A: Chemistry

journal homepage: www.elsevier.com/locate/jphotochem

Invited feature article

Facile synthesis of double cone-shaped $\text{Ag}_4\text{V}_2\text{O}_7/\text{BiVO}_4$ nanocomposites with enhanced visible light photocatalytic activity for environmental purification

Yang Hu^a, Jun Fan^a, Chenchen Pu^a, Hua Li^a, Enzhou Liu^{a,*}, Xiaoyun Hu^{b,*}^a School of Chemical Engineering, Northwest University, Xi'an 710069, China^b Department of Physics, Northwest University, Xi'an 710069, China

ARTICLE INFO

Article history:

Received 18 October 2016

Received in revised form 11 December 2016

Accepted 25 December 2016

Available online 27 January 2017

Keywords:

 BiVO_4 $\text{Ag}_4\text{V}_2\text{O}_7$

Double cone-shaped nanostructure

NO oxidation

Visible light photocatalyst

ABSTRACT

$\text{Ag}_4\text{V}_2\text{O}_7/\text{BiVO}_4$ photocatalysts with double cone-shaped nanostructure were successfully synthesized by a facile sodium polyphosphate-assisted hydrothermal method. The results demonstrate that coupling $\text{Ag}_4\text{V}_2\text{O}_7$ with BiVO_4 can promote the separation of photoinduced charge carriers and enhance the photon absorption efficiency. Experimental results indicate that $\text{Ag}_4\text{V}_2\text{O}_7/\text{BiVO}_4$ composites exhibit the enhanced photocatalytic activity for degradation of methylene blue (MB) and oxidation of NO in high concentrate (1600 ppb) compared to the pure BiVO_4 under visible light irradiation ($\lambda > 420$ nm). The composite with 0.08 mol% $\text{Ag}_4\text{V}_2\text{O}_7$ has the highest photocatalytic activity. MB degradation rate can reach 98.48% in 1 h and NO oxidation rate can reach 52.83% in 0.5 h on 0.08- $\text{Ag}_4\text{V}_2\text{O}_7/\text{BiVO}_4$, which are about 2.90 and 3.11 times higher than that of pure BiVO_4 respectively. The excellent activity can be attributed to the efficient charge transfer between $\text{Ag}_4\text{V}_2\text{O}_7$ and BiVO_4 , and active species h^+ and $^*\text{O}_2^-$ play important roles during MB degradation and NO oxidation. In addition, this composite exhibits favorable stability during the cycling experiment, suggesting it may be a promising visible light active photocatalyst for environmental applications.

© 2017 Elsevier B.V. All rights reserved.

1. Introduction

During the past decades, the application of semiconductor-based photocatalysis in hydrogen production from water splitting [1–4], degradation of organic pollutants in wastewater, removal of NO_x in air [5–10], and CO_2 reduction to obtain high valuable hydrocarbon fuels [11–15] has attracted considerable attention. Among various semiconductors investigated, TiO_2 has received far more attention in the photocatalysis field due to its low cost, low toxicity and high chemical stability [16–19]. However, the relatively wide band gap (3.2 eV for anatase, 3.0 eV for rutile) of TiO_2 limits its practical applications, which makes TiO_2 only respond to the ultraviolet (UV) light (about 4% of the solar energy) [20,21]. Therefore, great efforts have been devoted to develop the novel photocatalyst with highly visible light activity.

Bismuth vanadate (BiVO_4) has garnered considerable attention as a promising photocatalyst due to its excellent properties, such as

non-toxic, narrow band gap, good dispersibility, resistance to corrosion, and higher sunlight utilization [22–27]. There are three crystal structures of BiVO_4 according to the previous study, including monoclinic scheelite structure (ms- BiVO_4), tetragonal scheelite structure (ts- BiVO_4), and tetragonal zircon structure (tz- BiVO_4) [28,29]. Among these crystalline phases, ms- BiVO_4 exhibits much higher catalytic activity under visible light irradiation compared to ts- BiVO_4 and tz- BiVO_4 due to the effective hybridization of Bi 6s with O 2p to form the valence band with a narrower band gap ($E_g = 2.4$ eV) [30]. Recently, photocatalytic properties of BiVO_4 -based materials have been extensively explored.

It is well-known that the photocatalytic performance of BiVO_4 is strongly related to its morphology. For instance, Tan et al. prepared hierarchical structures of BiVO_4 via the microwave hydrothermal method. It is found that the BiVO_4 with different crystal phases and morphologies can be prepared by varying the pH values of the precursors, and the irregular rodlike ms- BiVO_4 obtained at pH 7.81 exhibited the best visible-light photocatalytic activity [31]. Ma et al. investigated ms- BiVO_4 samples prepared by a hydrothermal method. The results indicated that the morphology of the BiVO_4 greatly changed with the increase of ethylenediamine

* Corresponding authors.

E-mail addresses: liuenzhou@nwu.edu.cn (E. Liu), hxy3275@nwu.edu.cn (X. Hu).

tetraacetic acid (EDTA) amount. The obtained BiVO_4 with hollow polygon morphology showed higher discoloration rate of MB under simulated sunlight, 90.84% of MB could be degraded within 5 h [32]. Liu et al. discovered that the sheet-like BiVO_4 sample with highly exposed (010) facets could be obtained with assistance of glycerol, which exhibited the best photocatalytic performance for MB degradation [33]. Based on the above discussion, it can be concluded that morphology and microstructure have great effects on photocatalytic activity of BiVO_4 . Nevertheless, the reported BiVO_4 with rod-like [31], fusiform-like [32] and sheet-like [33] morphology showed low degradation rate under visible light irradiation, which usually takes about 3–5 h to completely discolor dyestuff. Therefore, the investigation on morphology of BiVO_4 would be beneficial to exploration of highly active BiVO_4 -based photocatalysts.

The activity of pristine ms- BiVO_4 is still low owing to the rapid recombination rate of electron-hole pairs and weak surface adsorption properties, which significantly limit its practical application. Previous studies had shown that composite photocatalysts could enlarge the spectral responsive range and promote the separation of photoinduced charge carriers, and thus could remarkably improve the photocatalytic activity of an individual semiconductor [34–38]. As a result, several BiVO_4 -based composites have been fabricated by coupling BiVO_4 with other semiconductors. For instance, Chang et al. described that the *p*- Co_3O_4 /*n*- BiVO_4 heterojunction can effectively suppress the excessive formation of recombination centers at interface and improve the surface reaction kinetics simultaneously. This composite achieved the highest photocurrent for water oxidation [39]. Wetchakun et al. prepared $\text{BiVO}_4/\text{CeO}_2$ nanocomposites by using precipitation method and hydrothermal techniques. The results clearly show that $\text{BiVO}_4/\text{CeO}_2$ nanocomposite with mol ratio of 0.6:0.4 exhibited the highest photocatalytic activity in dye wastewater treatment [40]. Li et al. synthesized the novel $\text{BiVO}_4/\text{FeVO}_4$ heterojunction photocatalysts by one-step hydrothermal method. The composites showed higher photocatalytic efficiency for the photodegradation activity of MNZ (metronidazole) under visible light irradiation, which was much higher than individual BiVO_4 or FeVO_4 [41]. In addition, other BiVO_4 -based composites such as $\text{BiVO}_4/\text{TiO}_2$ [42], $\text{V}_2\text{O}_5/\text{BiVO}_4$ [43], $\text{SnO}_2/\text{BiVO}_4$ [44], CuO/BiVO_4 [45], $\text{WO}_3/\text{BiVO}_4$ [46] and $\text{SiO}_2/\text{BiVO}_4$ [47] have also been reported. These studies show that the enhanced photoactivity results from a coupling effect between the two components in the composites, which can increase the electron transfer and inhibits the recombination of photo-generated charge carriers [44,48]. However, to the best of our knowledge, $\text{Ag}_4\text{V}_2\text{O}_7/\text{BiVO}_4$ photocatalyst has not been reported, and photocatalytic removal of high concentration NO in air using $\text{Ag}_4\text{V}_2\text{O}_7/\text{BiVO}_4$ composites under visible light irradiation has never been investigated.

In this work, we have successfully prepared a series of double cone-shaped $\text{Ag}_4\text{V}_2\text{O}_7/\text{BiVO}_4$ composites by a sodium polyphosphate-assisted hydrothermal method with an expectation to obtain a promising visible light driven catalyst. The as-obtained composite has been explored for the degradation of MB and oxidation of NO in high concentration under visible light irradiation ($\lambda > 420$ nm). The composite shows superior photocatalytic activity as compared with pure material. Moreover, the possible photocatalytic mechanism of the double cone-shaped $\text{Ag}_4\text{V}_2\text{O}_7/\text{BiVO}_4$ composites was also discussed.

2. Experimental section

All chemicals were of analytical reagent grade and used without further purification. Distilled water was used throughout.

2.1. The preparation of $\text{Ag}_4\text{V}_2\text{O}_7/\text{BiVO}_4$

The double cone-shaped $\text{Ag}_4\text{V}_2\text{O}_7/\text{BiVO}_4$ samples were prepared via hydrothermal process, the details of which are as follows: $\text{Bi}(\text{NO}_3)_3 \cdot 5\text{H}_2\text{O}$ was dissolved in 20 mL of HNO_3 (solution A) and NH_4VO_3 was dissolved in 20 mL of NaOH (solution B) respectively, the molar ratio of $\text{Bi}(\text{NO}_3)_3 \cdot 5\text{H}_2\text{O}$ and NH_4VO_3 is 1:1. Then a certain amount of surfactant sodium polyphosphate was added to solution B under stirring. The two solutions were magnetically stirred for 30 min at room temperature to obtain transparent solutions, then solution B was added dropwise into solution A under magnetic stirring to obtain a yellow homogeneous suspension. Subsequently, certain amount of AgNO_3 was added into the mixture. After further stirring for 2 h, the pH of the solution was adjusted to 7 by adding of NaOH solution, which was transferred into a 100 mL Teflon-lined stainless steel vessel, followed by heating at 180°C for 4 h. After cooled to room temperature naturally, the yellow precipitate was centrifuged, washed three times separately with distilled water and ethanol to remove the impurities. Finally, the obtained samples were dried in an oven at 60°C for 24 h. Briefly, the sample was denoted as 0.02- $\text{Ag}_4\text{V}_2\text{O}_7/\text{BiVO}_4$, 0.04- $\text{Ag}_4\text{V}_2\text{O}_7/\text{BiVO}_4$, 0.06- $\text{Ag}_4\text{V}_2\text{O}_7/\text{BiVO}_4$, 0.08- $\text{Ag}_4\text{V}_2\text{O}_7/\text{BiVO}_4$, 0.10- $\text{Ag}_4\text{V}_2\text{O}_7/\text{BiVO}_4$, 0.02, 0.04, 0.06, 0.08 and 0.10 represent the molar ratio of AgNO_3 to $\text{Bi}(\text{NO}_3)_3 \cdot 5\text{H}_2\text{O}$ in the starting materials, respectively. For comparison, pure double cone-shaped BiVO_4 was prepared without using AgNO_3 , and bulk-shaped BiVO_4 (BS- BiVO_4) was prepared in the absence of sodium polyphosphate and AgNO_3 . The synthesis process is illustrated in Fig. S1 of Supplementary material.

2.2. Characterization techniques

The morphologies were observed by a scanning electron microscopy (SEM, JSM-6390A) equipped with an energy-dispersive x-ray (EDS) analysis. The crystalline phases of the samples were identified by X-ray diffractometer (Shimadzu, XRD-6000, $\text{Cu K}\alpha$ radiation). UV-vis diffuse reflectance spectra were recorded on a Shimadzu UV-3600 spectrophotometer with an integrating sphere, and BaSO_4 was used as a reference. X-ray photoelectron spectroscopy was performed to examine the surface properties and composition (XPS, Kratos AXIS NOVA spectrometer). Photoluminescence (PL) spectra were obtained using a fluorescence spectrophotometer (Hitachi F-7000). The products of the photocatalytic oxidation of NO were analyzed by ion chromatography with ECD detector (DIONEX ICS-2100, AS18 as chromatographic column, 23 mmol L^{-1} of KOH solution as mobile phase).

2.3. Photocurrent-time measurement

Photocurrent-time measurements were performed on an electro-chemical analyzer (CHI660E, CHI Shanghai, Inc.) with a standard three electrode cell at room temperature. The prepared sample, saturated calomel electrode (SCE), and a Pt electrode were used as the working electrode, the reference electrode and the counter electrode, respectively. A 300 W Xe-lamp served as a light source, $0.1 \text{ M Na}_2\text{SO}_4$ aqueous solution was used as the electrolyte. The working electrodes were prepared as follows: Fluorine doped tin oxide (FTO) glass pieces ($2 \text{ cm} \times 3 \text{ cm}$) were cleaned successively by acetone and deionized water, and then dried in air. 5 mg of prepared sample was mixed with *N*-methyl-2-pyrrolidone to make slurry. Then the mixture was ultrasonicated for 1 h to obtain a suspension, which was coated onto the FTO glass substrate. The electrolyte was dried at 50°C for 6 h to obtain working electrode with a similar film thickness [49].

2.4. Photocatalytic degradation of MB

Photocatalytic degradation of MB was carried out to evaluate the performance of the samples. A 300 W Xe lamp with a visible light filter (>420 nm, 62.3 mW/cm²) was used as light source and the distance between the lamp and samples was about 10 cm. In a typical photocatalytic experiment, 50 mg of as-prepared photocatalyst was dispersed into 50 mL of 5 mg/L MB aqueous solution with constant magnetic stirring. The solution was stirred in the dark for 30 min prior to irradiation for establishing adsorption and desorption equilibrium. 3 mL of solution were taken out and centrifuged to remove the particles every 20 min, the concentration of MB was analyzed according to the absorption intensity at 664 nm with a Shimadzu UV-3600 spectrophotometer.

2.5. Photocatalytic removal of NO

The photocatalytic oxidation of NO was performed in a continuous flow reactor at room temperature. A schematic of the photocatalytic system is shown in the Supplementary material (Fig. S2). Briefly, the photocatalytic oxidation of NO experiments was controlled at the following condition: 0.2 g of as-prepared photocatalyst was dispersed in 20 mL of ethyl alcohol under ultrasonic condition for 20 min, and then the suspension was well dispersed into a dish with a diameter of 6.5 cm and dried at 60 °C, which was put into the center of a quartz reactor with inner volume of 380 cm³. A 300 W Xe lamp with a 420 nm filter was used

as visible light source. The gas mixture with 1600 ppb NO was fed into the reactor with a total flow rate of 300 mL min⁻¹, which was obtained by diluting NO in a compressed gas cylinder with 20 ppm N₂ balance. After the system was stable for 20 min, when the concentration of outlet NO is same with that of inlet gas, the lamp was turned on. The concentration of NO and NO₂ was continuously analyzed by electrochemical NO analyzer (Shenzhen Jishunan Technology CO. LTD., JSA9-NO) and NO₂ analyzer (JSA9-NO₂) at the outlet of the reaction system [6,50–52]. The conversion efficiency is defined as followings:

$$\text{NO conversion (\%)} = (C_0 - C) / C_0 \times 100\%$$

Where C is the outlet concentration of NO after reaction for time t, and C₀ represents the inlet concentration after achieving the adsorption–desorption equilibrium.

2.6. Active species analysis

Different radical scavengers, ethylenediamine tetraacetic acid (EDTA, scavenger of h⁺), benzoquinone (BQ, scavenger of •O₂⁻), Isopropanol (IPA, scavenger of •OH) was added to the reaction system under similar conditions. During photocatalytic degradation of MB, EDTA (0.1460 g, 10 mmol L⁻¹), BQ (0.0054 g, 1 mmol L⁻¹), IPA (3 mL) was added to the reaction system, respectively. In the process of sample preparation for photocatalytic oxidation of NO, 0.2 g of photocatalyst was dispersed in 20 mL of ethyl alcohol

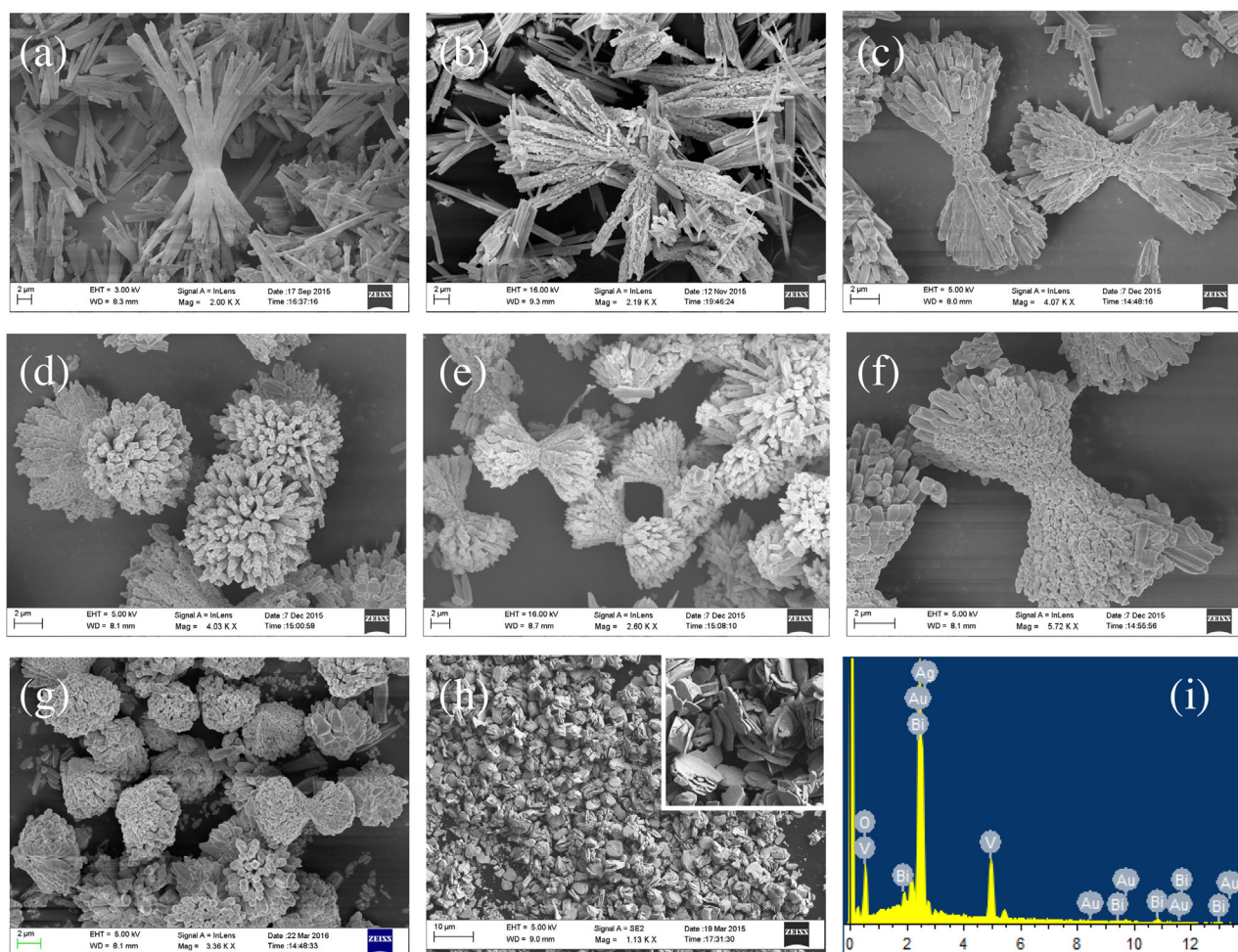


Fig. 1. SEM images of (a) pure BiVO₄; (b) 0.02-Ag₄V₂O₇/BiVO₄; (c–d) 0.04-Ag₄V₂O₇/BiVO₄; (e) 0.06-Ag₄V₂O₇/BiVO₄; (f) 0.08-Ag₄V₂O₇/BiVO₄; (g) 0.10-Ag₄V₂O₇/BiVO₄; (h) BS-BiVO₄; (i) EDS pattern of 0.08-Ag₄V₂O₇/BiVO₄ photocatalyst.

with EDTA (0.01 g) or BQ (0.01 g), and then the suspension was well dispersed into a dish with a diameter of 6.5 cm and dried at 60 °C. It is different to adding EDTA and BQ, 3 mL of IPA was dropwise added into the dried photocatalyst in the dish. Other conditions were the same as that in the 2.3 and 2.4 parts.

3. Results and discussions

3.1. Structure and morphology

3.1.1. SEM and EDS analysis

The morphology and size of the samples were characterized by SEM. Pure BiVO₄ displays a double cone-shaped morphology, which possesses smooth surface with approximately 10 μm in length (Fig. 1a). The SEM images of the Ag₄V₂O₇/BiVO₄ are shown in Fig. 1b–g. It is observed that the surface of BiVO₄ is covered by small particle and a rough surface was formed after adding AgNO₃ during preparation process. The increase of AgNO₃ resulted in the formation of more Ag₄V₂O₇ nanoparticles on BiVO₄. The detailed morphologies of the 0.04-Ag₄V₂O₇/BiVO₄ are shown in Fig. 1c and d. The overall view of Ag₄V₂O₇/BiVO₄ samples are double cone-shaped from the front with length of 6–8 μm (Fig. 1c), which is consist of irregularly nanorod observed from the side of the surface (Fig. 1d). However, when the molar ration of AgNO₃ to Bi(NO₃)₃·5H₂O increased to 0.1, the shape of the composite began to separate from each other, which was broken from the middle (Fig. 1g). Further investigation revealed that the formation of the above double cone-like structures depended on the existence of surfactant sodium polyphosphate, which plays an important role in the structure formation process. For comparison, Fig. 1h shows the SEM image of the BiVO₄ without surfactant sodium polyphosphate, it has bulk-shaped (marked as BS-BiVO₄). The composition of the Ag₄V₂O₇/BiVO₄ photocatalysts was further studied by energy-dispersive spectroscopy (EDS). As shown in Fig. 1i, which further verifies that Bi, V, Ag, and O as major elements in the Ag₄V₂O₇/BiVO₄ composites.

3.1.2. XRD analysis

Phase structures of the as-prepared samples were characterized by XRD. As shown in Fig. 2. All the diffraction peaks can be well indexed to monoclinic scheelite type BiVO₄ (JCPDS 14-0688), and the peaks of impurities Bi₂O₃ and V₂O₅ are not observed, indicating that BiVO₄ obtained by above hydrothermal method with high

purity and good crystallinity. The signals at 18.66°, 18.98°, 28.82°, 30.54°, 34.49°, 35.22°, 39.78°, 42.46°, 46.71°, 47.30°, 53.31°, 57.91° and 58.53° can be respectively indexed as (110), (011), (121), (040), (200), (002), (211), (051), (240), (042), (161), (170) and (321) planes of monoclinic BiVO₄ structure respectively. Weak diffraction peaks at 31.93° and 32.92° (marked with star) are detected in the XRD pattern of the composites in Fig. 2(c–f) after adding AgNO₃, which are corresponding to (224) and (040) facets of Ag₄V₂O₇ (JCPDS 77-0097), respectively. In addition, it can be seen that the diffraction of a series of as prepared Ag₄V₂O₇/BiVO₄ photocatalyst was similar to that of BiVO₄ sample. It is possibly due to the high crystallinity and content of the BiVO₄ in the samples, it has the dominant peaks in the XRD patterns of the composite samples [41]. As the molar ration AgNO₃ to Bi(NO₃)₃·5H₂O increases from 2% to 10%, the diffraction peaks of orthorhombic Ag₄V₂O₇ are gradually intensified. Nevertheless, the signals corresponding to the Ag₄V₂O₇ species were not observed in 0.02-Ag₄V₂O₇/BiVO₄ (Fig. 2b), which may be resulted from the low concentration. We also tried to prepare Ag₄V₂O₇ by the same method without adding Bi(NO₃)₃·5H₂O, the SEM, XRD and UV–vis diffuse reflectance spectra are shown in Figs. S3–S5. However, the sample obtained in our work is Ag₃VO₄ (JCPDS 43-0542) based on Fig. S4. It is hard to obtain pure Ag₄V₂O₇ (JCPDS 77-0097) using our method.

3.1.3. XPS analysis

The electronic state and composition of the double cone-shaped Ag₄V₂O₇/BiVO₄ samples were further evaluated by XPS. The XPS spectra demonstrated that the characteristic peaks of the Bi, V, O, Ag and C elements were detected obviously (Fig. 3a). The binding peak of C 1s at 284.61 eV originates from carbon in the instrument. In the XPS spectra, all peaks of the Bi, V, O, and Ag elements were calibrated according to the deviation between the C 1s peak and the standard binding energy of C 1s at 284.8 eV [53]. Fig. 3b shows the high resolution XPS spectrum of Bi 4f. Two peaks were detected with binding energy of 159 and 164.39 eV, corresponding to Bi 4f_{7/2} and Bi 4f_{5/2}, respectively, ascribed to Bi³⁺ in BiVO₄ [48]. In Fig. 3c, the peaks located at 516.65 and 524.19 eV are ascribed to V 2p_{1/2} and V 2p_{3/2} of V⁵⁺ species, respectively. The O 1s XPS spectrum is shown in Fig. 3d, two peaks at 530.18 and 532.38 eV are observed. The former is ascribed to the lattice oxide species, while the later is from the adsorbed oxygen species [54,55]. As illustrated in Fig. 3e, two typical peaks of Ag 3d can be observed, which corresponding to Ag 3d_{5/2} and 3d_{3/2}, respectively. Particularly, Ag 3d peaks can be further divided into four peaks by the XPS peak fitting program. The peaks at 367.8 and 373.8 eV originate from the Ag⁺ ion, and the peaks at 368.7 and 374.7 eV are assigned to metallic Ag⁰ species, respectively [56,57]. Thus, the XPS results further confirm that the double cone-shaped Ag₄V₂O₇/BiVO₄ nanocomposites can be fabricated via present method.

3.2. Optical properties

3.2.1. UV–vis diffuse reflectance spectra

Fig. 4 shows the typical UV–vis diffuse reflectance spectra of pure BiVO₄ and a series of as-prepared Ag₄V₂O₇/BiVO₄ samples. Apparently, all the samples exhibit excellent visible light absorption ability, which is attributed to the band–band electron transition of monoclinic BiVO₄ confirmed by XRD results (Fig. 2). As depicted in Fig. 4a, pure BiVO₄ displays significantly absorption from ultraviolet to 527 nm region. After the addition of AgNO₃ aqueous solution, the absorption edges of the samples extended to 560 nm. In addition, the absorption intensity of Ag₄V₂O₇/BiVO₄ samples increases with the increase of AgNO₃ concentration in the whole region.

The band gap energies (E_g) of BiVO₄ and Ag₄V₂O₇/BiVO₄ samples are calculated by the following formula:

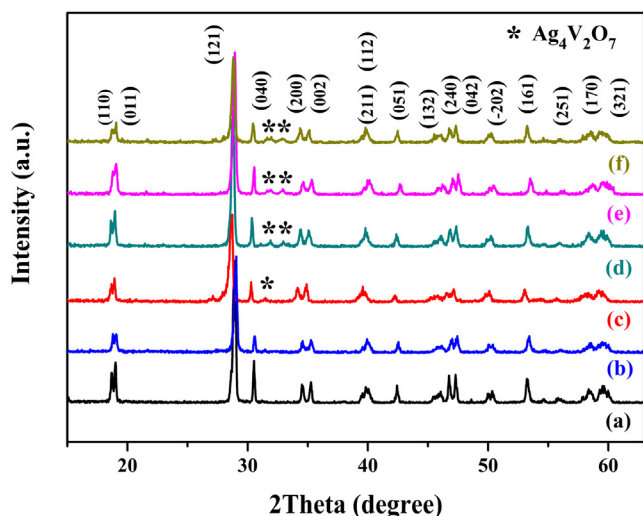


Fig. 2. XRD patterns of (a) pure BiVO₄; (b) 0.02-Ag₄V₂O₇/BiVO₄; (c) 0.04-Ag₄V₂O₇/BiVO₄; (d) 0.06-Ag₄V₂O₇/BiVO₄; (e) 0.08-Ag₄V₂O₇/BiVO₄; (f) 0.10-Ag₄V₂O₇/BiVO₄.

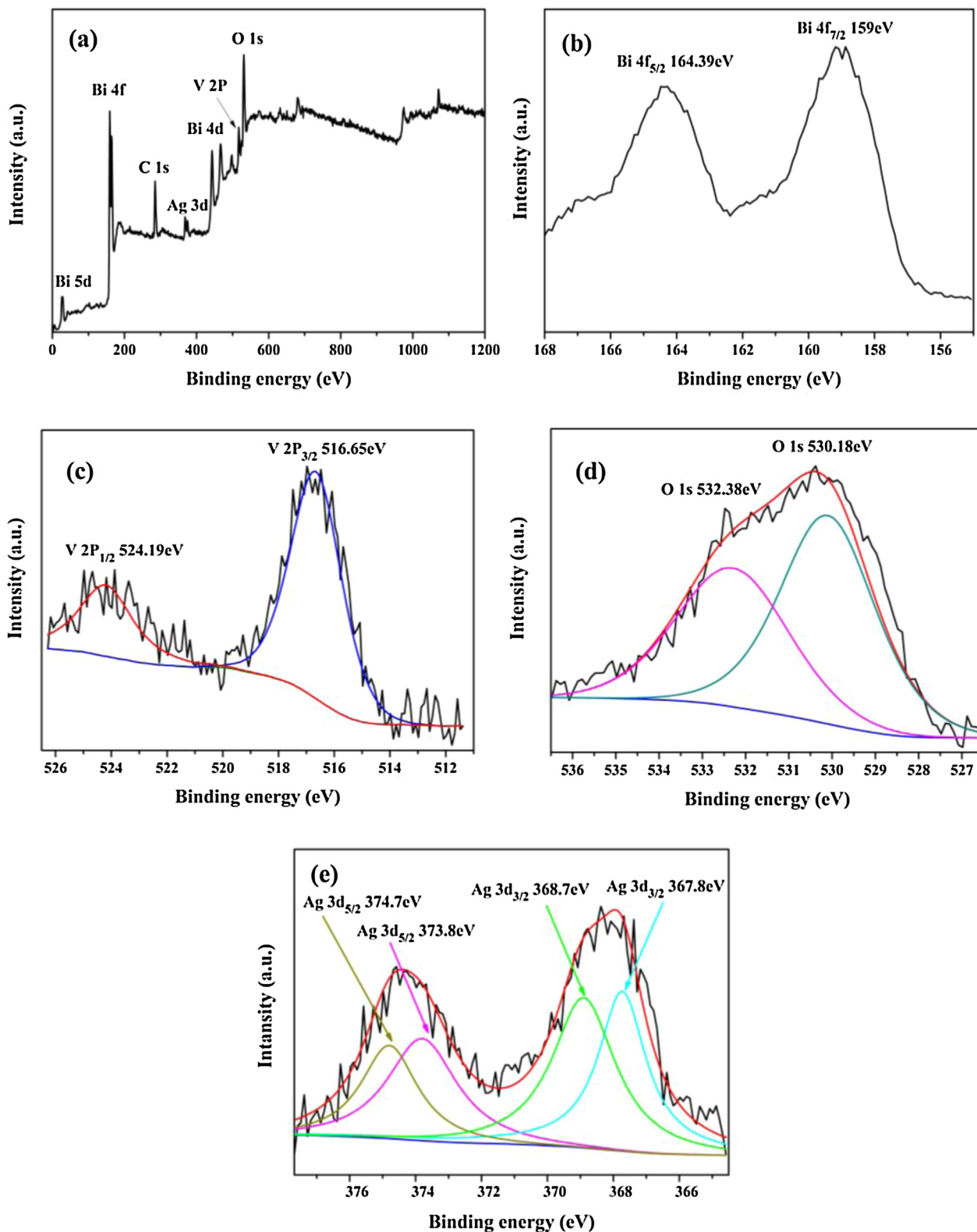


Fig. 3. XPS spectra of 0.08-Ag₄V₂O₇/BiVO₄ sample: (a) overall XPS spectra; (b) Bi 4f spectrum; (c) V 2p spectrum; (d) O 1s spectrum; (e) Ag 3d spectrum.

$$(\alpha h\nu) = A (h\nu - E_g)^n \quad (1)$$

Where α , ν , h , E_g and A are the absorption coefficients, the light frequency, Planck's constant, band gap and a constant, respectively. Among these parameters, n is determined by the type of optical transition of a semiconductor ($n=0.5$ for a direct transition and

$n=2$ for an indirect transition) [58,59]. For BiVO₄, n equals 0.5 for direct band gap materials. According to Eq. (1), the band gaps values for the samples can be estimated from a plot of $(\alpha h\nu)^2$ versus energy ($h\nu$) as presented in Fig. 4b. The straight line to the x axis will give a good approximation of the band gap energies for

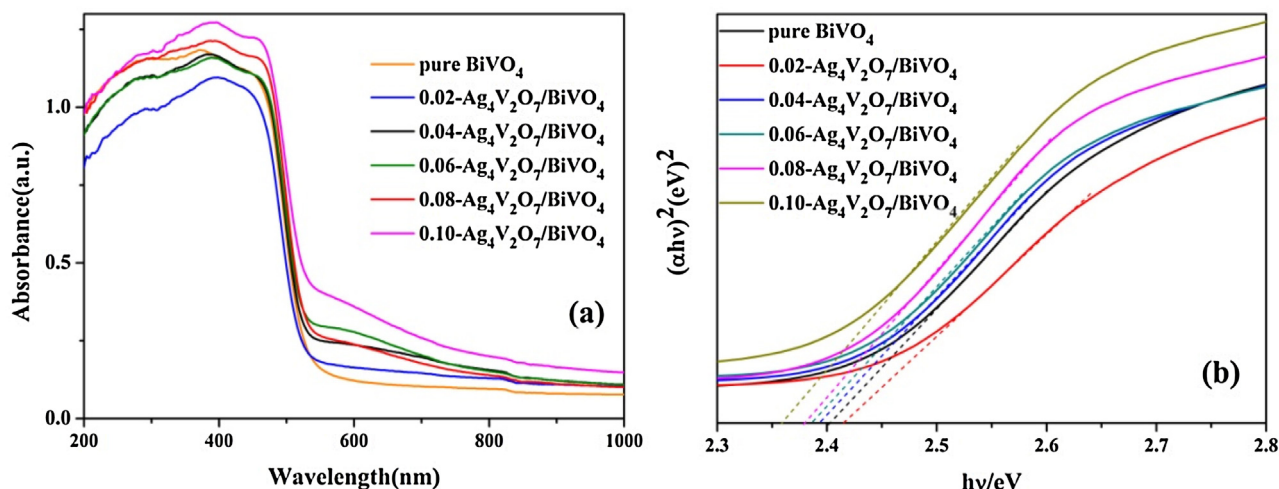


Fig. 4. (a) UV-vis diffuse reflectance spectra of $\text{Ag}_4\text{V}_2\text{O}_7/\text{BiVO}_4$ nanocomposites with different mole ratios; (b) plots of $(\alpha h\nu)^2$ versus $(h\nu)$ for samples with different mole ratios.

Table 1

Band gap values of as-synthesized samples.

Sample	Band gap/eV
Pure BiVO_4	2.40
0.02- $\text{Ag}_4\text{V}_2\text{O}_7/\text{BiVO}_4$	2.41
0.04- $\text{Ag}_4\text{V}_2\text{O}_7/\text{BiVO}_4$	2.39
0.06- $\text{Ag}_4\text{V}_2\text{O}_7/\text{BiVO}_4$	2.38
0.08- $\text{Ag}_4\text{V}_2\text{O}_7/\text{BiVO}_4$	2.37
0.10- $\text{Ag}_4\text{V}_2\text{O}_7/\text{BiVO}_4$	2.36

samples, the estimated E_g values of all samples are listed in Table 1, ranged from 2.41 eV to 2.36 eV, which is consistent with previous reports. Compared to pure double cone-shaped BiVO_4 samples, a weak redshift of band gap happens after the addition of AgNO_3 , the lower band gap energy indicates that the $\text{Ag}_4\text{V}_2\text{O}_7/\text{BiVO}_4$ samples can harvest more visible light and generate more electron-hole pairs, which could lead to higher photocatalytic performance.

3.2.2. Photoluminescence spectra and photocurrent measurements

Fig. 5a shows the comparison of PL spectra of the pure BiVO_4 and double cone-shaped $\text{Ag}_4\text{V}_2\text{O}_7/\text{BiVO}_4$ samples under the

excitation wavelength of 328 nm. It was clearly observed that the emission spectra of samples are similar, but the intensity is different. $\text{Ag}_4\text{V}_2\text{O}_7/\text{BiVO}_4$ sample exhibits much lower intensity than that of pure BiVO_4 . Possible explanation is that the combination of BiVO_4 and $\text{Ag}_4\text{V}_2\text{O}_7$ could promote the separation of the photogenerated electron-hole pairs and enhance the interfacial charge transfer efficiency, leading to the $\text{Ag}_4\text{V}_2\text{O}_7/\text{BiVO}_4$ sample with enhanced photocatalytic performance under visible light irradiation [60]. Photocurrent measurements were also carried out for BiVO_4 and 0.08- $\text{Ag}_4\text{V}_2\text{O}_7/\text{BiVO}_4$ composites via several switch-on and switch-off cycles to investigate the photo-induced charges separation efficiency. The measurements were carried out at 0.5 V vs SCE. As shown in Fig. 5b, an instantaneous rise in the photocurrent when the light source is turned on, and then a prompt recovery to the original value once the illumination is turned off. The changes of both “on” and “off” currents are nearly vertical, which indicates that charge transport in the as-prepared sample occurs very quickly [61,62]. The 0.08- $\text{Ag}_4\text{V}_2\text{O}_7/\text{BiVO}_4$ sample exhibits a higher photocurrent in comparison with pure BiVO_4 , implying that the introduction of $\text{Ag}_4\text{V}_2\text{O}_7$ is helpful in suppressing the recombination of electrons and holes, which is

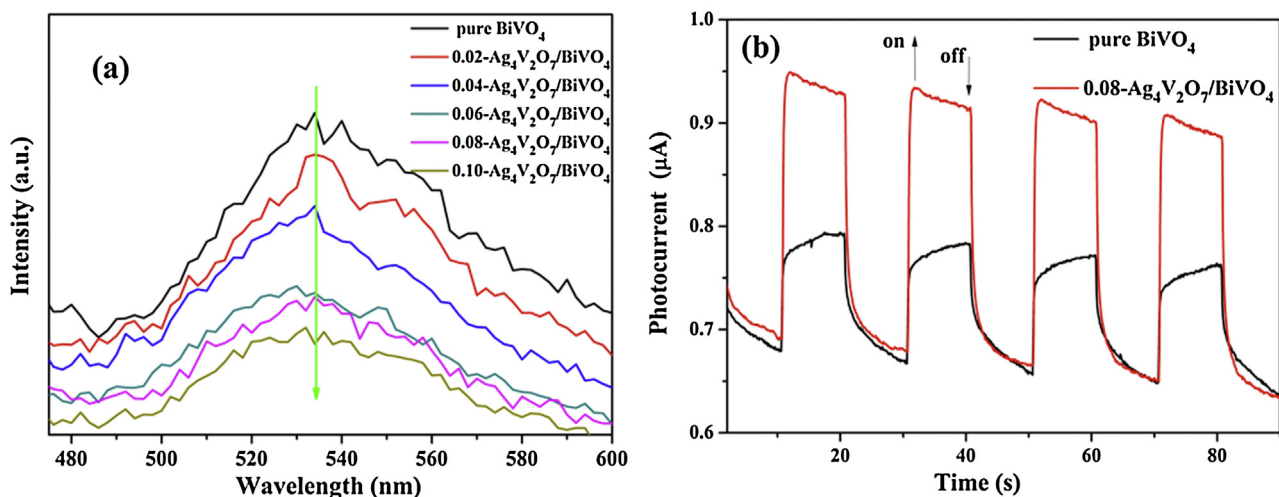


Fig. 5. (a) PL spectra of as-synthesized samples under the excitation wavelength of 328 nm; (b) transient photocurrent response of BiVO_4 and 0.08- $\text{Ag}_4\text{V}_2\text{O}_7/\text{BiVO}_4$ under visible light irradiation.

attributed to the efficient charge transfer between $\text{Ag}_4\text{V}_2\text{O}_7$ and BiVO_4 . This result is consistent with PL analyses.

3.3. Photocatalytic activity

3.3.1. Photocatalytic degradation of MB

The photocatalytic performances of the samples were evaluated by degradation of MB under visible light irradiation. The characteristic absorption of MB at about 664 nm was selected to monitor the photocatalytic degradation process (Fig. 6a). As depicted in Fig. 6b, most of the composites exhibit better photocatalytic activity than pure BiVO_4 , only 9.65% of the dye was degraded for 60 min without using any photocatalyst. The equilibrium adsorption quantity of $\text{Ag}_4\text{V}_2\text{O}_7/\text{BiVO}_4$ samples is higher than that of the pure BiVO_4 , which should be attributed to the rough surface of the composite photocatalysts. It is known that adsorption is the first step in photocatalytic process and the excellent adsorption property will benefit the photocatalytic performance [63]. For BS- BiVO_4 , 29.58% of MB is decreased after 60 min, but it reaches 79.41% after 60 min by pure double cone-shaped BiVO_4 . So, this new structure could enhance the photocatalytic activities of BiVO_4 . Furthermore, $\text{Ag}_4\text{V}_2\text{O}_7/\text{BiVO}_4$ displays remarkably higher photocatalytic activities than that of pure BiVO_4 . The 0.08- $\text{Ag}_4\text{V}_2\text{O}_7/\text{BiVO}_4$ sample exhibits the highest photocatalytic activity compared to the other tested photocatalysts, 98.48% of MB can be decreased on 0.08- $\text{Ag}_4\text{V}_2\text{O}_7/\text{BiVO}_4$

in 60 min, while the 0.02- $\text{Ag}_4\text{V}_2\text{O}_7/\text{BiVO}_4$, 0.04- $\text{Ag}_4\text{V}_2\text{O}_7/\text{BiVO}_4$, 0.06- $\text{Ag}_4\text{V}_2\text{O}_7/\text{BiVO}_4$ and 0.10- $\text{Ag}_4\text{V}_2\text{O}_7/\text{BiVO}_4$ composites remove 88.69%, 93.68%, 98.04% and 96.59% in the same time period, respectively.

To further investigate the photocatalytic performance, we estimated the reaction kinetics of the MB degradation. Fig. 6c shows the photodegradation kinetics of MB over the samples. It demonstrates the relationship between $\ln(C_0/C)$ and time by fitting the data in Fig. 6b. It is well known that when the pollutant is within the millimolar concentration range, photocatalytic oxidation of organic pollutants follows first-order kinetics, and the value of the rate constant k can be calculated by the following formula:

$$\ln(C_0/C) = kt \quad (2)$$

Where C_0 and C are the dye concentrations in solution at time 0 and t , respectively, and k is the apparent first-order rate constant [64]. As shown in Fig. 6c, the reaction rate constant k increases at first and then decreases with the increase of the $\text{Ag}_4\text{V}_2\text{O}_7$ concentration. It can be seen that the constants k for the MB degradation over 0.02- $\text{Ag}_4\text{V}_2\text{O}_7/\text{BiVO}_4$, 0.04- $\text{Ag}_4\text{V}_2\text{O}_7/\text{BiVO}_4$, 0.06- $\text{Ag}_4\text{V}_2\text{O}_7/\text{BiVO}_4$, 0.08- $\text{Ag}_4\text{V}_2\text{O}_7/\text{BiVO}_4$ and 0.10- $\text{Ag}_4\text{V}_2\text{O}_7/\text{BiVO}_4$ are about 1.37, 1.92, 2.79, 2.90 and 2.15 times higher than that of pure BiVO_4 , respectively. The constant k is the largest when the mole ratio of $\text{Ag}_4\text{V}_2\text{O}_7$ content is 0.08, indicating that 0.08- $\text{Ag}_4\text{V}_2\text{O}_7/\text{BiVO}_4$ sample gives the highest rate constant for MB dye degradation under visible light irradiation. It is well-known that the

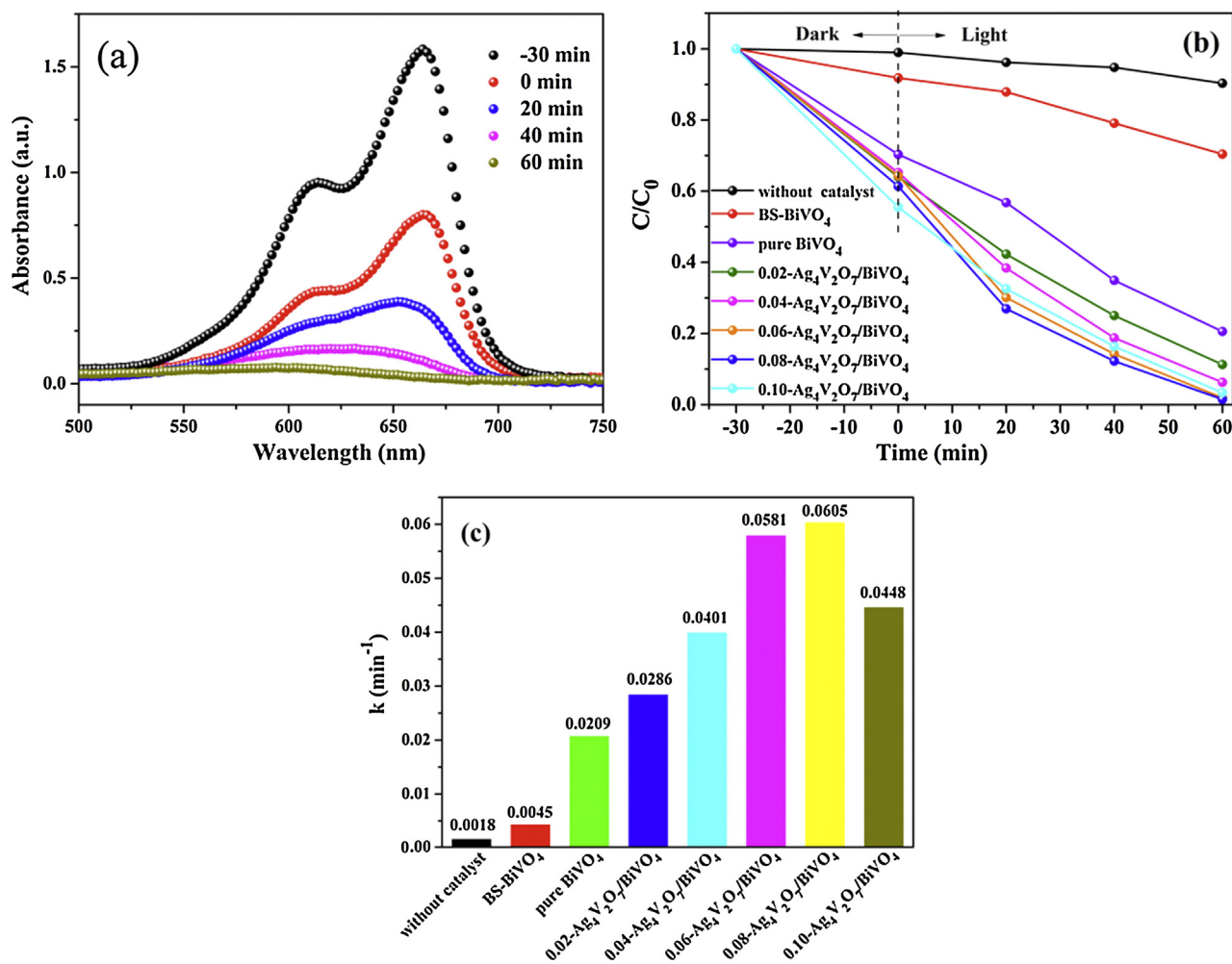


Fig. 6. (a) Absorption spectra of solution of MB in the presence of 0.08- $\text{Ag}_4\text{V}_2\text{O}_7/\text{BiVO}_4$ under visible light irradiation at different times; (b) comparison of photocatalytic degradation efficiency of MB under visible light on all photocatalysts; (c) Plot of the rate constant k for degradation of MB over different samples under visible light irradiation.

photocatalytic performance of BiVO_4 is strongly related to its morphology and microstructure, the nanoparticles keep original double cone shape for 0.02- $\text{Ag}_4\text{V}_2\text{O}_7/\text{BiVO}_4$, 0.04- $\text{Ag}_4\text{V}_2\text{O}_7/\text{BiVO}_4$, 0.06- $\text{Ag}_4\text{V}_2\text{O}_7/\text{BiVO}_4$ and 0.08- $\text{Ag}_4\text{V}_2\text{O}_7/\text{BiVO}_4$, while for 0.1 or higher $\text{Ag}_4\text{V}_2\text{O}_7/\text{BiVO}_4$, the original shape were broken, as shown in Fig. 1 g, which could be the reason that the activity of 0.1- $\text{Ag}_4\text{V}_2\text{O}_7/\text{BiVO}_4$ decreases after introducing more $\text{Ag}_4\text{V}_2\text{O}_7$. Besides, the active sites of BiVO_4 might be covered by more $\text{Ag}_4\text{V}_2\text{O}_7$ particles.

In view of practical applications, the stability and recyclability of the catalysts are also indispensable for photocatalysts. The lifetime of catalysts was also evaluated by using 0.08- $\text{Ag}_4\text{V}_2\text{O}_7/\text{BiVO}_4$ sample to react with MB. The degradation rate of MB can be well remained after four recycles photocatalytic experiment under visible light illumination. It can be seen that no significant loss in photocatalytic activity is observed (Fig. 7a). The XRD pattern and SEM image of photocatalyst (Fig. 7b and c) reveal that the structure and the phase of the photocatalyst remains intact. Above result shows that the $\text{Ag}_4\text{V}_2\text{O}_7/\text{BiVO}_4$ photocatalyst can work as a stable and efficient visible light photocatalyst.

3.3.2. Photocatalytic removal of NO

To evaluate their potential ability for air purification, the double cone-shaped $\text{Ag}_4\text{V}_2\text{O}_7/\text{BiVO}_4$ composites were employed to NO in gas phase. Fig. 8a shows the conversion of NO with the time of irradiation under visible light irradiation over different samples. As

shown in Fig. 8a, NO conversion efficiency increases gradually with irradiation time over all the photocatalysts and then reaches a steady state concentration [65]. The possible reasons are as follows: at the beginning of the photocatalytic reaction, lots of NO is adsorbed on the surface of the catalyst with strong adsorption ability until equilibrium achieved. Then NO are oxidized to NO_2 along with the prolonging of reaction time along, then NO_2 adsorbs on the surface of the samples and occupies active sites. Therefore, the conversion efficiency of NO decreased until approached a steady state [10,50]. Pure double cone-shaped BiVO_4 exhibits a relatively low NO conversion rate (16.98%). The photocatalytic oxidation ability of NO greatly improved with the further increase $\text{Ag}_4\text{V}_2\text{O}_7$ content. The NO conversion for 0.02- $\text{Ag}_4\text{V}_2\text{O}_7/\text{BiVO}_4$, 0.04- $\text{Ag}_4\text{V}_2\text{O}_7/\text{BiVO}_4$, 0.06- $\text{Ag}_4\text{V}_2\text{O}_7/\text{BiVO}_4$, 0.08- $\text{Ag}_4\text{V}_2\text{O}_7/\text{BiVO}_4$ and 0.10- $\text{Ag}_4\text{V}_2\text{O}_7/\text{BiVO}_4$ composites at 30 min is 19.81%, 32.64%, 41.04%, 52.83% and 46.56% in the same time period, respectively. And the optimal sample is 0.08- $\text{Ag}_4\text{V}_2\text{O}_7/\text{BiVO}_4$, its photocatalytic oxidation rate is nearly 3.11 times higher than that of pure sample. The significant improvement of NO conversion shows that the combination of $\text{Ag}_4\text{V}_2\text{O}_7$ with BiVO_4 can significantly enhance the photocatalytic activity of BiVO_4 .

To further investigate the photocatalytic performance of the samples, first order rate constants were calculated based on the experimental data. The results are shown in Fig. 8b. It can be clearly seen that the constants k for oxidation of NO over 0.02- $\text{Ag}_4\text{V}_2\text{O}_7/$

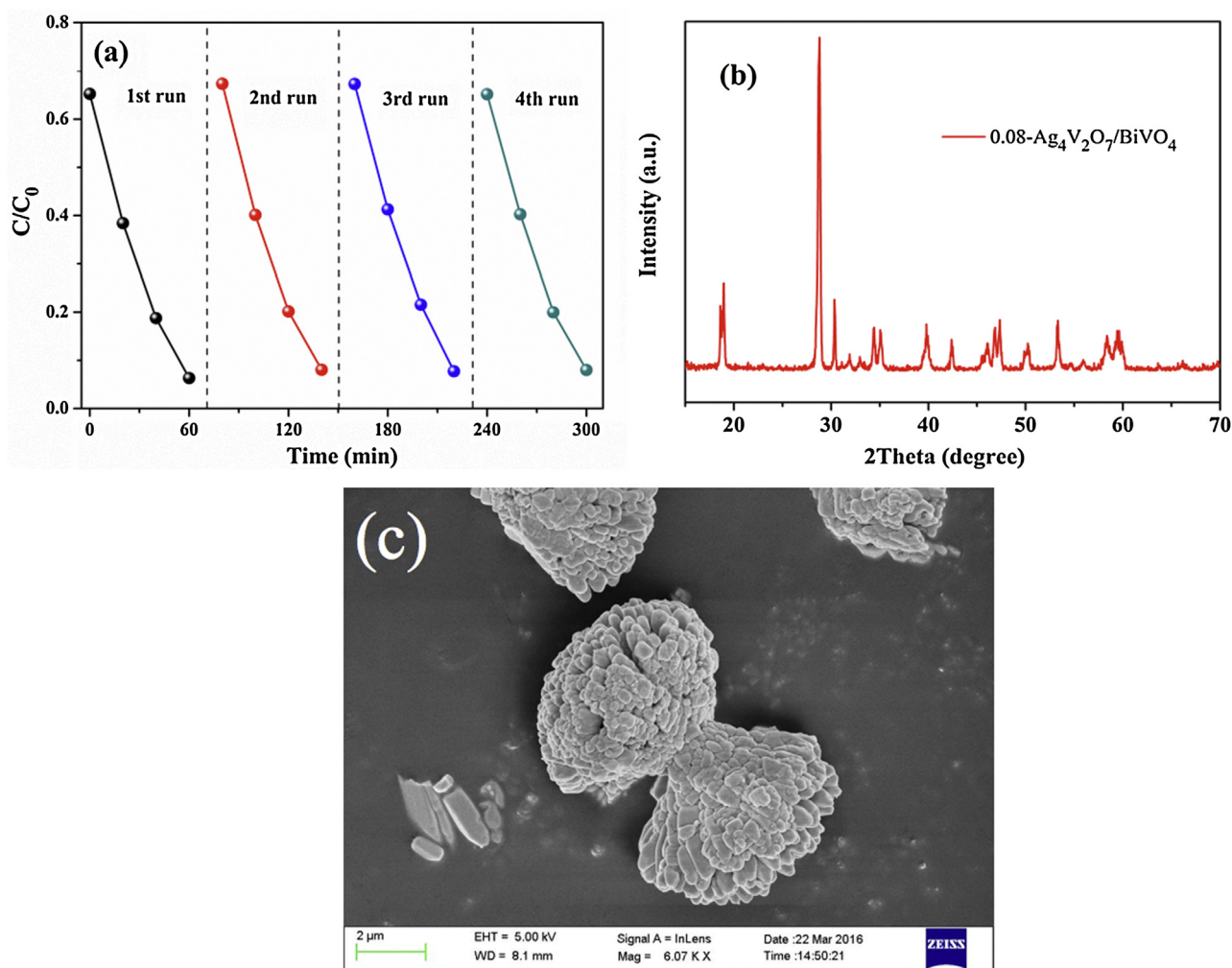


Fig. 7. (a) Cycling runs for the photocatalytic degradation of MB over 0.08- $\text{Ag}_4\text{V}_2\text{O}_7/\text{BiVO}_4$ sample under visible light irradiation; (b) XRD patterns of used 0.08- $\text{Ag}_4\text{V}_2\text{O}_7/\text{BiVO}_4$; (c) SEM image of used 0.08- $\text{Ag}_4\text{V}_2\text{O}_7/\text{BiVO}_4$.

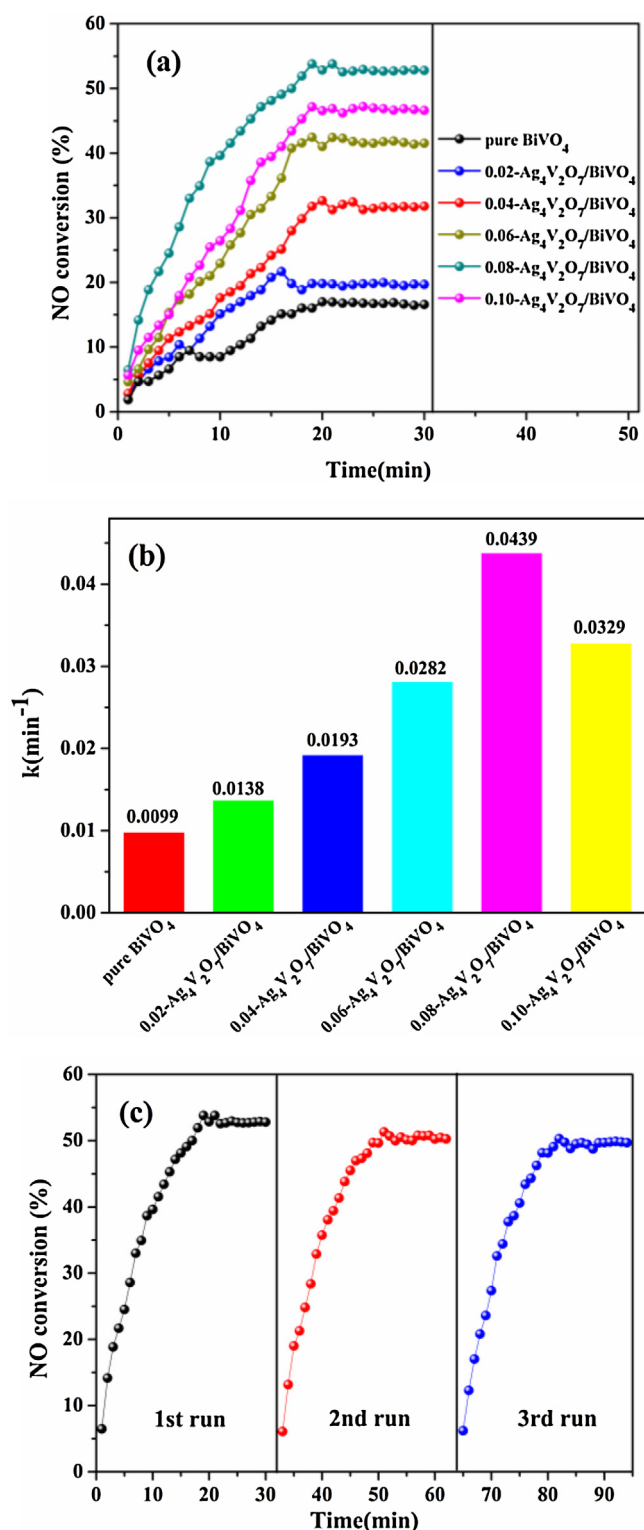


Fig. 8. (a) Variations of NO conversion efficiency with the time of irradiation using different samples under visible light irradiation; (b) reaction rate constant (min^{-1}) of the as-prepared photocatalysts. (c) cycling runs for the photocatalytic oxidation of NO over 0.08-Ag₄V₂O₇/BiVO₄ under visible light irradiation.

BiVO₄, 0.04-Ag₄V₂O₇/BiVO₄, 0.06-Ag₄V₂O₇/BiVO₄, 0.08-Ag₄V₂O₇/BiVO₄ and 0.10-Ag₄V₂O₇/BiVO₄ catalysts are about 1.40, 1.95, 2.85, 4.43 and 3.32 times higher than that of pure BiVO₄ (0.0099 min^{-1}) respectively, indicating that 0.08-Ag₄V₂O₇/BiVO₄ sample gives the highest rate constant for NO removal under visible light

irradiation. Fig. 8c shows after 3 successive NO degradation under visible light illumination, the photocatalytic activities of the 0.08-Ag₄V₂O₇/BiVO₄ is obviously stable, no significant loss in photocatalytic activity is observed.

A possible process of photocatalytic removal of NO is as follows using $\cdot\text{OH}$ as oxidizing agent. It is reported that the photo-generated reactive radicals generated on the surface of the photocatalyst was able to oxidize NO to NO₂⁻ and NO₃⁻ [66–68]. At the end of reaction, the catalyst was washed with 10 mL of water, and then it was centrifuged to obtain the supernatant, HNO₃ (0.6937 ppm) was detected in the supernatant by ion chromatography (IC), suggesting that NO₃⁻ exists in the solution. Besides, NO₂⁻ was not detected by IC. These results could be attributed to the rate of Reactions (4) and (5) is very quickly that of Reaction (3). NO₂ and HNO₂ are intermediate products. They may be oxide to HNO₃ immediately after generation, so NO₂⁻ is hard to detect. Therefore, HNO₃ is the main products during the photocatalytic oxidation of NO over Ag₄V₂O₇/BiVO₄, it is consistent with the previous report [69].



3.3.3. Active species analysis

In general, several reactive intermediate species such as h^+ , $\cdot\text{O}_2^-$ and $\cdot\text{OH}$ may be involved in the photocatalytic decompositions of dyes and NO. To further insight on the degradation mechanism, the role of the reactive species responsible for degradation of MB and oxidation of NO was determined using a series of scavengers [70]. Fig. 9 shows plot of the rate constant for the degradation reaction in presence of the selected scavengers. The rate constant for degradation of MB (Fig. 9a) without using any scavenger (0.05945 min^{-1}) decreases to 0.0045 min^{-1} , 0.032 min^{-1} , and 0.0421 min^{-1} in the presence of ethylenediamine tetraacetic acid (EDTA, scavenger of h^+), benzoquinone (BQ, scavenger of $\cdot\text{O}_2^-$), Isopropanol (IPA, scavenger of $\cdot\text{OH}$), respectively. The rate constant for oxidation of NO (Fig. 9b) without using any scavenger (0.0439 min^{-1}) decreases to 0.0114 min^{-1} , 0.0205 min^{-1} , and 0.0419 min^{-1} , respectively. It was apparent that all these scavengers could partially suppress the reaction. The decrease of the degradation rate constant in presence of EDTA is much higher than those of other scavengers. So, the role of the reactive species is as the following sequence: holes > superoxide radicals > hydroxyl radicals. Therefore, it is concluded that holes play a key role during the photocatalytic decompositions of MB and oxidation of NO [71].

As we all known, BiVO₄ and Ag₄V₂O₇ are both visible light photocatalysts. The composites exhibit the enhanced photocatalytic activity for degradation of methylene blue (MB) dye molecules and oxidation of NO under visible light irradiation. In addition, we also synthesized BiVO₄/TiO₂ composite as shown in Fig. S6. The photoactivity of BiVO₄/TiO₂ is very poor than that of Ag₄V₂O₇/BiVO₄ under visible light irradiation (data not shown), because TiO₂ only respond to UV light, the efficiency of photocatalytic activity is limited by its wide bandgap (3.2 eV). Besides, BiVO₄/TiO₂ has also been reported in recent years. Natda Wetchakun et al. synthesized BiVO₄/TiO₂ nanocomposites. The mole ratio of BiVO₄/TiO₂ at 0.5:0.5 provided the highest photocatalytic activity, the highest MB degradation of 84% was obtained within 120 min of simulated solar light irradiation [34]. In this

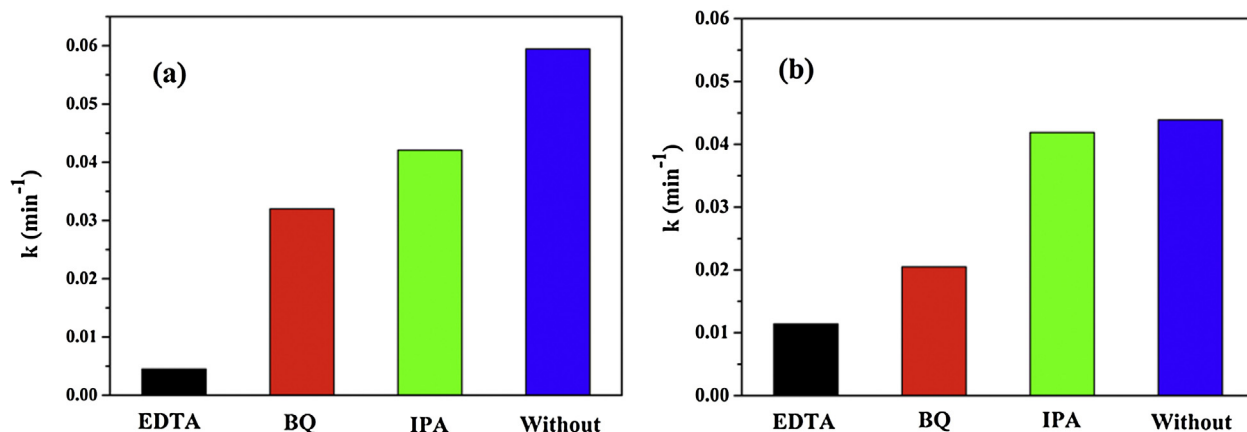


Fig. 9. (a) MB degradation rate constants over 0.08-Ag₄V₂O₇/BiVO₄ in presence of various scavengers; (b) NO oxidation rate constants over 0.08-Ag₄V₂O₇/BiVO₄ in presence of various scavengers.

work, the 0.08-Ag₄V₂O₇/BiVO₄ sample exhibited 98.48% MB decomposition in 60 min.

3.4. Theoretical calculation

Furthermore, the photocatalytic property of the photocatalyst is associated with its band gap structure. In order to clarify the enhanced photocatalytic mechanism over the composite photocatalyst, it is necessary to find out the conduction band edge (E_{CB}) and valence band edge (E_{VB}) of the catalysts. The E_{CB} and E_{VB} of a semiconductor are calculated according to the following empirical formula:

$$E_{VB} = X + 0.5Eg - E^e \quad (6)$$

$$E_{CB} = E_{VB} - Eg \quad (7)$$

$$X = [\chi(A)^a \chi(B)^b \chi(C)^c]^{1/(a+b+c)} \quad (8)$$

Where E_{VB} is the VB edge potentials, E_{CB} is the CB edge potential, Eg is the band gap energy of the semiconductor, X is the electronegativity of the semiconductor (a , b , c are the atomic number of compounds), E^e is the energy of free electrons vs. hydrogen (4.5 eV) [72]. The band gap energy of BiVO₄ and Ag₄V₂O₇ is 2.40 eV and 2.50 eV, respectively. According to the X and Eg values, the E_{CB} value of BiVO₄ was calculated to be 0.45 eV, and the E_{VB} value of BiVO₄ was estimated to be 2.86 eV. The VB holes of BiVO₄ own a large oxidation power for the oxidation of organic pollutants owing to the high potential. The E_{CB} and the E_{VB} of Ag₄V₂O₇ were determined to be -0.03 and 2.46 eV, respectively (as shown in Table 2).

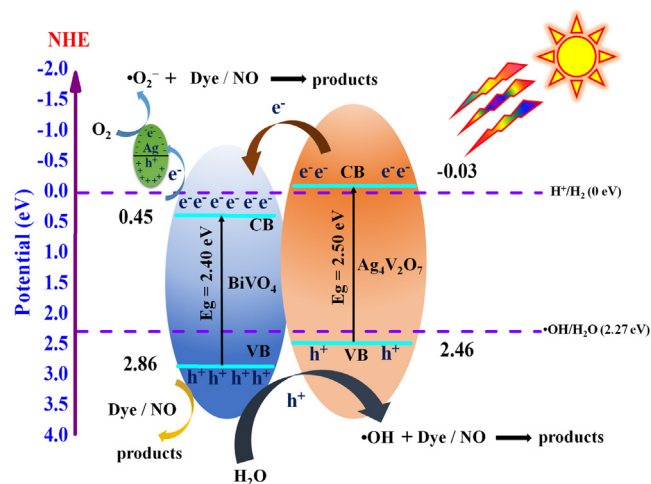
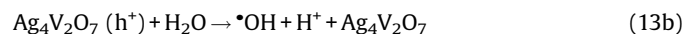
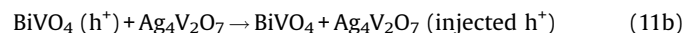
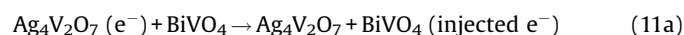
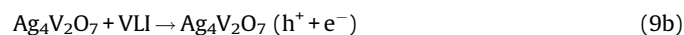
3.5. Photocatalytic mechanism

Based on the experimental results, a possible pathway for the photocatalytic degradation of MB and the removal of NO in the presence of Ag₄V₂O₇/BiVO₄ composite under visible light

Table 2
The VB and CB edge positions of BiVO₄ and Ag₄V₂O₇ estimated by empirical formula.

Semiconductor	X/eV	Eg/eV	E _{VB} /eV	E _{CB} /eV
BiVO ₄	6.16	2.40	2.86	0.45
Ag ₄ V ₂ O ₇	5.72	2.50	2.46	-0.03

irradiation (VLI) was proposed, and the applicable reactions are given as follows:



Scheme 1. Possible photocatalytic mechanism for degradation of MB and oxidation of NO over Ag₄V₂O₇/BiVO₄ under visible light irradiation.



In accordance with Reactions (9a)–(14), a possible mechanism is proposed and illustrated in Scheme 1. When the $\text{Ag}_4\text{V}_2\text{O}_7/\text{BiVO}_4$ photocatalyst was subjected to visible light irradiation, both BiVO_4 and $\text{Ag}_4\text{V}_2\text{O}_7$ can be excited and produce photogenerated electron–hole pairs (Formulas (9a) and (9b)). Under normal situation, most of electron–hole pairs recombine rapidly (Formula (10)), making pure BiVO_4 with low photocatalytic activity. Considering the relative positions of the CB and VB edges, the conduction band potential of $\text{Ag}_4\text{V}_2\text{O}_7$ were more negative than that of BiVO_4 , the photo-induced electrons could migrate from $\text{Ag}_4\text{V}_2\text{O}_7$ to the BiVO_4 surface (Formula (11a)). At the same time, h^+ produced by BiVO_4 transfer to the valence band of $\text{Ag}_4\text{V}_2\text{O}_7$ (Formula (11b)), which avoid recombination between the excited electrons and holes. Thus, BiVO_4 and $\text{Ag}_4\text{V}_2\text{O}_7$ have the suitable conduction and valence band levels for promoting charge separation at the composite photocatalysts interfaces [73]. In addition, Ag nanoparticles are also excited due to the localized SPR and generate electron–hole pairs under visible light irradiation (Formula (12)). The photo-generated electrons in Ag nanoparticles and those transferred from BiVO_4 could be trapped by O_2 to form $\bullet\text{O}_2^-$ reactive oxygen species, which further reacts with MB/NO (Formula (13a)) [74,75]. However, the CB of BiVO_4 (0.456 eV) shows a poor reduction power and are not enough to reduce O_2 to $\bullet\text{O}_2^-$ radicals because the reduction potential of $\text{O}_2/\bullet\text{O}_2^-$ is -0.33 eV [76]. Meanwhile, the photogenerated holes on the surface of $\text{Ag}_4\text{V}_2\text{O}_7$ can directly oxidize water and/or hydroxyl ions to give $\bullet\text{OH}$ radicals ($E(\bullet\text{OH}/\text{H}_2\text{O})=2.27$ eV, $E(\bullet\text{OH}/\text{OH}^-)=2.38$ eV) to decompose MB in the aqueous solution or to oxidize NO to NO_2^- and NO_3^- (Formula (13b)). Moreover, the photogenerated holes could oxidize the dye molecules directly on $\text{Ag}_4\text{V}_2\text{O}_7$ surfaces (Formula (14)). As a consequence, photogenerated holes played a significant role during the whole photocatalytic degradation, which is consistent with the fact that EDTA is demonstrated as the most efficient scavenger to inhibit the oxidative reaction by consuming the formed holes. Therefore, this high photocatalytic performance is attributed to the positive effects between the photocatalysis of $\text{Ag}_4\text{V}_2\text{O}_7/\text{BiVO}_4$ composite catalysts.

4. Conclusions

In summary, highly efficient visible-light-driven photocatalysts of $\text{Ag}_4\text{V}_2\text{O}_7/\text{BiVO}_4$ nanocomposites with double cone-shaped were successfully synthesized by a facile hydrothermal method. We found that $\text{Ag}_4\text{V}_2\text{O}_7/\text{BiVO}_4$ heterojunction displayed excellent visible light harvesting property, lower recombination rate of photo-generated electrons and holes, and higher degradation rate for MB and higher removal rate for NO. MB degradation rate can reach 98.48% in 1 h and NO oxidation rate can reach 52.83% in 0.5 h on 0.08- $\text{Ag}_4\text{V}_2\text{O}_7/\text{BiVO}_4$, which are about 2.90 and 3.11 times higher than that of pure BiVO_4 respectively. h^+ and $\bullet\text{O}_2^-$ as active species play important roles during MB degradation and NO oxidation. The enhancement could be mainly attributed to the effective separation of photogenerated electrons across the $\text{Ag}_4\text{V}_2\text{O}_7/\text{BiVO}_4$ heterojunction. This work provides a new insight on developing active BiVO_4 -based photocatalysts and demonstrates the great potential of using $\text{Ag}_4\text{V}_2\text{O}_7/\text{BiVO}_4$ heterojunction for efficient environmental remediation.

Acknowledgments

This work was supported by the National Natural Science Foundation of China (21306150, 21476183, 21676213 and 51372201), Project funded by China Postdoctoral Science

Foundation (2016M600809), the Specialized Research Fund for the Doctoral Program of Higher Education of China (20136101110009), the Shaanxi Provincial Research Foundation for Basic Research (2015JM5159), and the Scientific Research Starting Foundation of Northwest University (PR12216).

Appendix A. Supplementary data

Supplementary data associated with this article can be found, in the online version, at <http://dx.doi.org/10.1016/j.jphotochem.2016.12.035>.

References

- [1] Y. Matsumoto, U. Unal, N. Tanaka, A. Kudo, H. Kato, *J. Solid State Chem.* 177 (2004) 4205–4212.
- [2] H. Jung, S.Y. Chae, C. Shin, B.K. Min, O.S. Joo, Y.J. Hwang, *ACS Appl. Mater. Interfaces* 7 (2015) 5788–5796.
- [3] Y.H. Ng, A. Iwase, A. Kudo, R. Amal, *J. Phys. Chem. Lett.* 1 (2010) 2607–2612.
- [4] J. Yuan, J. Wen, Y. Zhong, X. Li, Y. Fang, S. Zhang, W. Liu, *J. Mater. Chem. A* 3 (2015) 18244–18255.
- [5] Y. Hu, D. Li, H. Wang, G. Zeng, X. Li, Y. Shao, *J. Mol. Catal. A–Chem.* 408 (2015) 172–178.
- [6] M. Ou, Q. Zhong, S. Zhang, H. Nie, Z. Lv, W. Cai, *Appl. Catal. B–Environ.* 193 (2016) 160–169.
- [7] T. Saison, N. Chemin, C. Chanéac, O. Durupthy, L. Mariey, F. Maugé, V. Brezová, J.-P. Jolivet, *J. Phys. Chem. C* 119 (2015) 12967–12977.
- [8] L. Xia, J. Bai, J. Li, Q. Zeng, X. Li, B. Zhou, *Appl. Catal. B–Environ.* 183 (2016) 224–230.
- [9] Y. Hu, D. Li, F. Sun, H. Wang, Y. Weng, W. Xiong, Y. Shao, *RSC Adv.* 5 (2015) 54882–54889.
- [10] X. Song, Y. Hu, M. Zheng, C. Wei, *Appl. Catal. B–Environ.* 182 (2016) 587–597.
- [11] L. Ye, H. Wang, X. Jin, Y. Su, D. Wang, H. Xie, X. Liu, X. Liu, *Sol. Energy Mater. Sol. Cells* 144 (2016) 732–739.
- [12] S. Das, W.M.A. Wan Daud, *Renew. Sust. Energy Rev.* 39 (2014) 765–805.
- [13] J.Y. Do, V. Tamilavan, R. Agneeswari, M.H. Hyun, M. Kang, *J. Photochem. Photobiol. A* 330 (2016) 30–36.
- [14] E. Liu, Y. Hu, H. Li, C. Tang, X. Hu, J. Fan, Y. Chen, J. Bian, *Ceram. Int.* 41 (2015) 1049–1057.
- [15] L. Zhang, W. Wang, D. Jiang, E. Gao, S. Sun, *Nano Res.* 8 (2015) 821–831.
- [16] Z. Zhang, Z. Wang, S.-W. Cao, C. Xue, *J. Phys. Chem. C* 117 (2013) 25939–25947.
- [17] J. Wen, X. Li, W. Liu, Y. Fang, J. Xie, Y. Xu, *Chin. J. Catal.* 36 (2015) 2049–2070.
- [18] H. Zhang, Y. Sheng, X. Zhou, Y. Song, Z. Shi, X. Xu, H. Zou, *Powder Technol.* 274 (2015) 193–198.
- [19] X. Li, J. Yu, M. Jaroniec, *Chem. Soc. Rev.* 45 (2016) 2603–2636.
- [20] E. Liu, L. Kang, F. Wu, T. Sun, X. Hu, Y. Yang, H. Liu, J. Fan, *Plasmonics* 9 (2014) 61–70.
- [21] Y. Liu, H. Tang, H. Lv, P. Zhang, Z. Ding, S. Li, J. Guang, *Powder Technol.* 283 (2015) 246–253.
- [22] K. Wang, L. Liang, H. Liu, X. Xie, Q. Hao, C. Liu, *Mater. Lett.* 161 (2015) 336–339.
- [23] D. Kang, Y. Park, J.C. Hill, K.S. Choi, *J. Phys. Chem. Lett.* 5 (2014) 2994–2999.
- [24] X. Lin, X. Guo, W. Shi, F. Guo, G. Che, H. Zhai, Y. Yan, Q. Wang, *Catal. Commun.* 71 (2015) 21–27.
- [25] C.N. Van, W.S. Chang, J.-W. Chen, K.-A. Tsai, W.-Y. Tzeng, Y.-C. Lin, H.-H. Kuo, H.-J. Liu, K.-D. Chang, W.-C. Chou, C.-L. Wu, Y.-C. Chen, C.-W. Luo, Y.-J. Hsu, Y.-H. Chu, *Nano Energy* 15 (2015) 625–633.
- [26] Y. Zhang, Z. Yi, G. Wu, Q. Shen, *J. Photochem. Photobiol. A* 327 (2016) 25–32.
- [27] B. Liu, Z. Wang, S. Zhou, J. He, *Mater. Lett.* 160 (2015) 218–221.
- [28] Y. Lu, Y.-S. Luo, D.-Z. Kong, D.-Y. Zhang, Y.-L. Jia, X.-W. Zhang, *J. Solid State Chem.* 186 (2012) 255–260.
- [29] S.M. Thalluri, S. Hernández, S. Bensaid, G. Saracco, N. Russo, *Appl. Catal. B–Environ.* 180 (2016) 630–636.
- [30] Y. Xue, X. Wang, *Int. J. Hydrogen Energy* 40 (2015) 5878–5888.
- [31] G. Tan, L. Zhang, H. Ren, S. Wei, J. Huang, A. Xia, *ACS Appl. Mater. Interfaces* 5 (2013) 5186–5193.
- [32] W. Ma, Z. Li, W. Liu, *Ceram. Int.* 41 (2015) 4340–4347.
- [33] W. Liu, G. Zhao, M. An, L. Chang, *Appl. Surf. Sci.* 357 (2015) 1053–1063.
- [34] N. Wetchakun, S. Chainet, S. Phanichphant, K. Wetchakun, *Ceram. Int.* 41 (2015) 5999–6004.
- [35] K.-H. Ye, Z. Chai, J. Gu, X. Yu, C. Zhao, Y. Zhang, W. Mai, *Nano Energy* 18 (2015) 222–231.
- [36] H. Fan, D. Wang, Z. Liu, T. Xie, Y. Lin, *Dalton Trans.* 44 (2015) 11725–11731.
- [37] S. Sun, W. Wang, *RSC Adv.* 4 (2014) 47136–47152.
- [38] X. Li, T. Xia, C. Xu, J. Murowchick, X. Chen, *Catal. Today* 225 (2014) 64–73.
- [39] X. Chang, T. Wang, P. Zhang, J. Zhang, A. Li, J. Gong, *J. Am. Chem. Soc.* 137 (2015) 8356–8359.
- [40] N. Wetchakun, S. Chainet, B. Inceesungvorn, K. Pingmuang, S. Phanichphant, A.I. Minett, J. Chen, *ACS Appl. Mater. Interfaces* 4 (2012) 3718–3723.
- [41] J. Li, W. Zhao, Y. Guo, Z. Wei, M. Han, H. He, S. Yang, C. Sun, *Appl. Surf. Sci.* 351 (2015) 270–279.
- [42] M. Xie, Y. Feng, X. Fu, P. Luan, L. Jing, *J. Alloys Compd.* 631 (2015) 120–124.

- [43] J. Su, X.-X. Zou, G.-D. Li, X. Wei, C. Yan, Y.-N. Wang, J. Zhao, L.-J. Zhou, J.-S. Chen, *J. Phys. Chem. C* 115 (2011) 8064–8071.
- [44] J. Yin, S. Huang, Z. Jian, Z. Wang, Y. Zhang, *Mater. Sci. Semicond. Process.* 34 (2015) 198–204.
- [45] C. Yu, K. Yang, C.Y. Jimmy, F. Cao, X. Li, X. Zhou, *J. Alloys Compd.* 509 (2011) 4547–4552.
- [46] J. Su, L. Guo, N. Bao, C.A. Grimes, *Nano Lett.* 11 (2011) 1928–1933.
- [47] S.K. Pilli, T.G. Deutsch, T.E. Furtak, J.A. Turner, L.D. Brown, A.M. Herring, *Phys. Chem. Chem. Phys.* 14 (2012) 7032–7039.
- [48] A.Y. Booshehri, S. Chun-Kiat Goh, J. Hong, R. Jiang, R. Xu, *J. Mater. Chem. A* 2 (2014) 6209.
- [49] Y. He, L. Zhang, M. Fan, X. Wang, M.L. Walbridge, Q. Nong, Y. Wu, L. Zhao, *Sol. Energy Mater. Sol. Cell* 137 (2015) 175–184.
- [50] T. Wu, X. Li, D. Zhang, F. Dong, S. Chen, *J. Alloys Compd.* 671 (2016) 318–327.
- [51] C. Tang, E. Liu, J. Fan, X. Hu, Y. Ma, J. Wan, *RSC Adv.* 5 (2015) 91979–91987.
- [52] Z. Zhao, W. Zhang, Y. Sun, J. Yu, Y. Zhang, H. Wang, F. Dong, Z. Wu, *J. Phys. Chem. C* 120 (2016) 11889–11898.
- [53] J. Xu, W. Wang, J. Wang, Y. Liang, *Appl. Surf. Sci.* 349 (2015) 529–537.
- [54] J. Zhang, B. Wang, C. Li, H. Cui, J. Zhai, Q. Li, *J. Environ. Sci.* 26 (2014) 1936–1942.
- [55] S. Yang, Y. Feng, J. Wan, W. Zhu, Z. Jiang, *Appl. Surf. Sci.* 246 (2005) 222–228.
- [56] R. Qiao, M. Mao, E. Hu, Y. Zhong, J. Ning, Y. Hu, *Inorg. Chem.* 54 (2015) 9033–9039.
- [57] J. Li, M. Cui, Z. Guo, Z. Liu, Z. Zhu, *Mater. Interfaces* 151 (2015) 75–78.
- [58] X. Lin, Y. Wang, J. Zheng, C. Liu, Y. Yang, G. Che, *Dalton Trans.* 44 (2015) 19185–19193.
- [59] X. Lin, X. Guo, W. Shi, L. Zhao, Y. Yan, Q. Wang, *J. Alloys Compd.* 635 (2015) 256–264.
- [60] X. Gao, Z. Wang, F. Feng, W. Li, *Mater. Sci. Semicond. Process.* 35 (2015) 197–206.
- [61] Y. Yin, E. Liu, H. Li, C. Tang, C. Pu, *Ceram. Int.* 42 (2016) 9387–9395.
- [62] L. Huang, Y. Li, H. Xu, Y. Xu, J. Xia, K. Wang, H. Li, X. Cheng, *RSC Adv.* 3 (2013) 22269–22279.
- [63] Y. Geng, P. Zhang, N. Li, Z. Sun, *J. Alloys Compd.* 651 (2015) 744–748.
- [64] X. Lin, F. Huang, W. Wang, Y. Wang, Y. Xia, J. Shi, *Appl. Catal. A-Gen.* 313 (2006) 218–223.
- [65] N.H. Nguyen, H. Bai, *Appl. Surf. Sci.* 355 (2015) 672–680.
- [66] M. Takeuchi, H. Yamashita, M. Matsuoka, *Catal. Lett.* 67 (2000) 135–137.
- [67] J.K. Sikkema, S.K. Ong, J.E. Alleman, *Constr. Build. Mater.* 100 (2015) 305–314.
- [68] S. Devahasdin, C. Fan, K. Li, *J. Photochem. Photobiol. A-Chem.* 156 (2003) 161–170.
- [69] M. Ou, Q. Zhong, S. Zhang, L. Yu, *J. Alloys Compd.* 626 (2015) 401–409.
- [70] M. Shekofteh-Gohari, A. Habibi-Yangjeh, *Solid State Sci.* 48 (2015) 177–185.
- [71] F. Kiantazh, A.H. Yangjeh, *Mater. Sci. Semicond. Process.* 39 (2015) 671–679.
- [72] W. Zhao, Y. Guo, Y. Faiz, W.-T. Yuan, C. Sun, S.-M. Wang, Y.-H. Deng, Y. Zhuang, Y. Li, X.-M. Wang, *Appl. Catal. B-Environ.* 163 (2015) 288–297.
- [73] R. Ran, J.G. McEvoy, Z. Zhang, *Mater. Res. Bull.* 74 (2016) 140–150.
- [74] Y. Sang, Y. Huang, W. wang, Z. Fang, B. Geng, *RSC Adv.* 5 (2015) 39651–39656.
- [75] Z. Wei, L. Feng, J. Zhi-Ming, S. Xiao-Bo, Y. Peng-Hui, W. Xue-Ren, S. Cheng, G. Zhan-Qi, L. Liang-Sheng, *J. Mater. Chem. A* 2 (2014) 13226.
- [76] Y. Xu, M. Lv, H. Yang, Q. Chen, X. Liu, F. Wei, *RSC Adv.* 5 (2015) 43473–43479.